

Supplementary Information:
Exciton transport in molecular organic semiconductors boosted
by transient quantum delocalization

Samuele Giannini^{1, †,*}, Wei-Tao Peng¹, Lorenzo Cupellini², Daniele Padula³, Antoine Carof⁴, and Jochen Blumberger^{1,*}

¹Department of Physics and Astronomy and Thomas Young Centre, University College London, London WC1E 6BT, UK.

[†]Current address: Laboratory for Chemistry of Novel Materials, University of Mons, Mons 7000, Belgium

²Dipartimento di Chimica e Chimica Industriale, Università di Pisa, Via G. Moruzzi 13, 56124 Pisa, Italy

³Dipartimento di Biotecnologie, Chimica e Farmacia, Università di Siena, Via A. Moro 2, 53100, Siena, Italy.

⁴Laboratoire de Physique et Chimie Théoriques, CNRS, UMR No. 7019, Université de Lorraine, BP 239, 54506 Vandoeuvre-lés-Nancy Cedex, France.

*Corresponding Authors, e-mail: samuele.giannini.16@ucl.ac.uk (S.G.),
j.blumberger@ucl.ac.uk (J.B)

1 Excitation energies

The vertical excitation energies as well as the adiabatic excitation energies for the lowest singlet excited state (S1) of ANT, a6T, PDI, DCVSN5 and Y6 molecules are reported in Table 1. These data refer to optimized geometries of the single molecules in gas-phase.

Table 1: Excitation and reorganization energies (eV) for the lowest-energy (singlet) state of ANT, a6T, PDI, DCVSN5 and Y6.^a

	Functional	S1 vert.	f^c	S1 adiab.	S1 Exp. ^d	λ^{XT}
ANT	CAM-B3LYP	3.70	0.086	3.41	3.3-3.4	0.572
	ω B97X-D	3.71	0.089	3.43		0.561
a6T ^b	CAM-B3LYP	2.96	2.042	2.68	2.5	0.558
	ω B97X-D	3.03	2.060	2.74		0.562
PDI	CAM-B3LYP	2.85	0.752	2.65	2.37	0.390
	ω B97X-D	2.89	0.758	2.68		0.405
DCVSN5	CAM-B3LYP	2.79	2.049	2.64	2.13	0.294
	ω B97X-D	2.86	2.061	2.69		0.320
Y6	CAM-B3LYP	2.35	2.421	2.23	1.70	0.250
	ω B97X-D	2.45	2.436	2.32		0.267

^a Basis set is fixed to 6-31g(d,p) as commonly used in the literature for similar systems¹⁻⁴. ^b The geometry for a6T was kept coplanar as done in Ref.² since oligothiophenes tend to crystallize in the solid state with coplanar thiophene units². ^c The calculated oscillator strengths are reported in a.u. ^d Experimental values are taken for solution and gas-phase molecules from Ref.^{5,6} in the case of ANT, Ref.^{7,8} for a6T, Ref.⁹ for a similar PDI derivative, Ref¹⁰ for DCVSN5 and Ref.¹¹ for Y6.

The first important observation is the fact the two long-range corrected functionals give very similar values both for energies and oscillator strengths (f) of the lowest-energy excitations of the different systems, pointing to a robust description of the transition density of these excitations by different functionals. As the following calculations are aimed at estimating correctly electronic couplings, as explained in the main text, a good evaluation of the transition densities is the most important issue. It is also worth noting that the second lowest (singlet) excited state as found from both functionals is about 0.5-1.0 eV above S1. This means that the Frenkel approximation describing the excited state of the system as a combination of locally excited S1 states is a good first approximation to study transport properties in these OSs.

We also plot the Natural Transition Orbitals (NTOs)¹² corresponding to the S1 excited state in Figure 1 of the main text for all the investigated molecules. The NTOs offer a useful way of visualizing which orbitals give the largest contribution to a given single-particle excitation (the NTOs are obtained here by using the NTOBuilder tool¹³). For all systems we can see that the NTOs with the largest contributions are indeed essentially the same as the HOMO and LUMO orbitals of the single molecules.

2 Excitonic couplings

We analyse here various flavours of the excitonic coupling approaches as defined in the main text. The electronic coupling is one of the main ingredients of the Frenkel exciton Hamiltonian employed in this work. We evaluated excitonic couplings using the full Coulomb integral, V_{Coulomb} , in Eq. 10 main text, the TrESP approach, V_{TrESP} , in Eq. 11 main text and the point-dipole approximation (PDA), V_{PDA} , in Eq. 8 below, for all the systems considered here. These values have been compared with the total excitonic coupling, V , obtained using the multi-state fragment excitation difference fragment charge difference approach (MS-FED-FCD) described in Section 2.1. The objective is to assess the extent of the short-range coupling in these closely packed OS solids and the different levels of approximation of the long-range Coulomb interaction. We note in passing that, to check the quality of the TrESP charges found from the ESP fitting procedure (as described in the main text), we have made sure that the sum of the TrESP charges is zero (as it would be the case if the full transition density were integrated over all space) and also that the dipole moments obtained directly from the charge densities, $\mu = \int d\mathbf{r}_I \rho^T(\mathbf{r}_I) \mathbf{r}_I$, are identical with those calculated from the atomic TrESP charges, $\mu = \sum_I q_I \mathbf{r}_I$ (see also Section 2.6).

For the calculation of MS-FED-FCD couplings (V) and Coulomb contributions (V_{Coulomb}) we have used CAM-B3LYP¹⁴ functional for a6T, PTCDI-H and Y6 (as suggested in Ref.^{4,15}) and ω B97X-D¹⁶ for ANT and DCVSN5 (for a more consistent comparison with Ref¹). The results are reported in Table 1 for three of the closest crystal pairs of the investigated OSs. As reported in the main text, we observe that V_{Coulomb} is generally very close to the total coupling V . The mean relative unsigned error (MRUE) is about 0.7%. This small discrepancy can be attributed to the missing short-range part, V_{Short} . The observation that $V \approx V_{\text{Coulomb}}$ lays the groundwork for efficient approximations of the long-range Coulomb interaction using TrESP charges (see below).

Notably, we also found that the two long-range corrected functionals give very similar values for the Coulomb couplings of the analysed systems (e.g. maximum discrepancies less than 5 meV in a6T). This is because the transition densities are described similarly by both functionals.

2.1 Multi-state FED-FCD

In this section we present two useful diabaticization schemes: the fragment charge difference (FCD)^{17,18} and the fragment excitation difference (FED)¹⁹ methods, and their combination in the general multi-state FED-FCD (MS-FED-FCD) scheme,²⁰⁻²² used in this work to obtain total excitonic couplings (V in the main text) between maximally localized Frenkel exciton states, that can be used as a benchmark for more approximate methods as discussed in the main text.

We start by considering the case of a dimer composed of two molecules donor (k) and acceptor (l). The FED scheme can recover the diabatic (localized) basis from delocalized excited states by using an

additional operator Δx , which measures the difference in excitation number between the donor (k) and acceptor (l) molecules. The elements of the Δx matrix are given in terms of "excitation densities", defined as the sum of attachment (electron) and detachment (hole) densities²³:

$$\Delta x_{ij} = \int_{\mathbf{r} \in k} \rho_{ij}^{\text{ex}}(\mathbf{r}) d\mathbf{r} - \int_{\mathbf{r} \in l} \rho_{ij}^{\text{ex}}(\mathbf{r}) d\mathbf{r} \quad (1)$$

where i and j are two adiabatic states and ρ_{ij}^{ex} is the excitation density, defined as,

$$\rho_{ij}^{\text{ex}}(\mathbf{r}) = \rho_{ij}^{\text{Att}}(\mathbf{r}) + \rho_{ij}^{\text{Det}}(\mathbf{r}) \quad (2)$$

The quantity Δx has its extrema when the excitation is entirely localized on either the donor (k) or acceptor (l). Without loss of generality, assuming that the adiabatic states i and j are the combination of two diabatic states, $|k^*l\rangle$ localized on k , and $|kl^*\rangle$ localized on l , the eigenvectors of the 2×2 Δx matrix represent the transformation from the adiabatic to the diabatic basis (\mathbb{U}), and the eigenvalues are either 1 or -1 for $|k^*l\rangle$ and $|kl^*\rangle$ ^{19,20,24}. The diagonal matrix of adiabatic energies (\mathbb{H}^{ad}) can be transformed into the diabatic basis of $|k^*l\rangle$ and $|kl^*\rangle$ by $\mathbb{U}^\dagger \mathbb{H}^{\text{ad}} \mathbb{U} = \mathbb{H}$. The electronic coupling between these states is found as the off-diagonal element of \mathbb{H} .

The same strategy can be applied to computing the coupling to charge transfer (CT) states. The FCD method uses an additional operator Δq to localize the electronic charge:¹⁷

$$2\Delta q_{ij} = \int_{\mathbf{r} \in k} \rho_{ij}(\mathbf{r}) d\mathbf{r} - \int_{\mathbf{r} \in l} \rho_{ij}(\mathbf{r}) d\mathbf{r} \quad (3)$$

where $\rho_{ij}(r)$ is the transition density between states j and i , if $j \neq i$, and the state density if $j = i$. Similarly to the FED case, the matrix Δq can be diagonalized to obtain locally excited states (such as kl^* and k^*l) with eigenvalue 0, and CT states, such as k^-l^+ or k^+l^- , with eigenvalues 1 or -1 , respectively. This is similar to the FED when the adiabatic states are combination of only two diabatic states. However, in the systems analysed in this work a 2 state diabatization procedure is not sufficient to retrieve excitonic couplings between completely de-mixed and localized (Frenkel) exciton states, which in our case, form the state space for the Frenkel Hamiltonian in Eq. 2 main text (see also Section 2.2 below).

To overcome this limitation we employed a multi-state FED-FCD procedure. This approach is a generalization of the FED and FCD methods just described^{18,20,24} and can make use of multiple adiabatic eigenstates of the donor-acceptor supermolecular system to recover maximally localized and decoupled diabatic states. This strategy was previously successfully employed to recover excitonic couplings in light-harvesting and biological systems^{20,21} as well as bridged donor-acceptor moieties²⁴. For a more detailed description of this approach we refer to Ref.^{18,20}. In brief this algorithm starts from the definitions of the additional operators Δx and Δq defined before. For CT states such as k^-l^+ and k^+l^- Δx should be zero,

while $\Delta q = \pm 1$ (albeit small numerical uncertainties,¹⁸). On the contrary, for localized Frenkel-Exciton (XT) states such as kl^* and k^*l , Δx equals +1 and -1, respectively, and $\Delta q = 0$. We can define the matrix

$$\mathbb{D} = (\Delta q)^2 - (\Delta x)^2 \quad (4)$$

which then has eigenvalues +1 and -1, respectively for subspaces of CT and XT states. The first step of the multi-FCD-FED scheme is to diagonalize \mathbb{D} to separate CT and XT subspaces, similarly to multi-state FCD (previously developed in Ref.¹⁸) :

$$\mathbb{U}_1 \mathbb{D} \mathbb{U}_1^\dagger = \mathbb{D}' \quad (5)$$

The same transformation \mathbb{U}_1 is applied to Δx and Δq , to obtain $\Delta x'$ and $\Delta q'$. Now, the states can be assigned as either CT or XT depending on the value of \mathbb{D}' . $\Delta x'$ and $\Delta q'$ can be each diagonalized within the XT and CT subspaces respectively, so that:

$$\begin{aligned} \mathbb{U}_2 \Delta x' \mathbb{U}_2^\dagger &= \Delta x'' \\ \mathbb{U}_2 \Delta q' \mathbb{U}_2^\dagger &= \Delta q'' \end{aligned} \quad (6)$$

where $\Delta x''$ is diagonal only in the XT block, whereas $\Delta q''$ is diagonal only in the CT block. \mathbb{U}_2 is block diagonal and rotates the XT and CT subspaces separately. Within the XT subspace, the diagonal values of $\Delta x''$ can be used to separate kl^* (XT1) states from k^*l (XT2) states. At the same time, $\Delta q''$ can be used to divide CT states in k^-l^+ (CT1) and k^+l^- (CT2). At this point, the four subspaces have been separated. The diagonal electronic Hamiltonian \mathbb{E} can be transformed to this basis as $\mathbb{U}_2 \mathbb{U}_1 \mathbb{E} \mathbb{U}_1^\dagger \mathbb{U}_2^\dagger = \mathbb{H}''$. Finally, we require that the Hamiltonian of each subspace is diagonal, *i.e.* that the states of the same subspace are not coupled to each other.¹⁸

$$\mathbb{U}_3 \begin{pmatrix} \mathbb{H}''_{CT1} & \mathbb{H}''_{CT1,CT2} & \mathbb{H}''_{CT1,XT1} & \mathbb{H}''_{CT1,XT2} \\ \mathbb{H}''_{CT2,CT1} & \mathbb{H}''_{CT2} & \mathbb{H}''_{CT2,XT1} & \mathbb{H}''_{CT2,XT2} \\ \mathbb{H}''_{XT1,CT1} & \mathbb{H}''_{XT1,CT2} & \mathbb{H}''_{XT1} & \mathbb{H}''_{XT1,XT2} \\ \mathbb{H}''_{XT2,CT1} & \mathbb{H}''_{LH2,CT2} & \mathbb{H}''_{XT2,XT1} & \mathbb{H}''_{XT2} \end{pmatrix} \mathbb{U}_3^\dagger = \begin{pmatrix} \epsilon''_{CT1} & \mathbb{H}''_{CT1,CT2} & \mathbb{H}''_{CT1,XT1} & \mathbb{H}''_{CT1,XT2} \\ \mathbb{H}''_{CT2,CT1} & \epsilon''_{CT2} & \mathbb{H}''_{CT2,XT1} & \mathbb{H}''_{CT2,XT2} \\ \mathbb{H}''_{XT1,CT1} & \mathbb{H}''_{XT1,CT2} & \epsilon''_{XT1} & \mathbb{H}''_{XT1,XT2} \\ \mathbb{H}''_{XT2,CT1} & \mathbb{H}''_{LH2,CT2} & \mathbb{H}''_{XT2,XT1} & \epsilon''_{XT2} \end{pmatrix} \quad (7)$$

The unitary matrix \mathbb{U}_3 is block diagonal, and each block of \mathbb{U}_3 diagonalizes each of the CT1, CT2, XT1, and XT2 blocks of the Hamiltonian. The final Hamiltonian \mathbb{H}''' in Eq. 7 contains the diabatic energies ϵ on the diagonal, and the electronic couplings in the off-diagonal blocks.

2.2 The importance of including multiple states in MS-FED-FCD diabaticization

It is important to note that in many cases, and also for the systems investigated in this work, a 2 state adiabatic basis, employed in the diabaticization procedure to calculate the reference coupling V , is not sufficient to retrieve the coupling between completely localized states. In fact, often the adiabatic states

are linear combination of a number of diabatic states of both donor and acceptor. Moreover, charge-transfer states can mix with Frenkel exciton states, and vice-versa^{18,24}. To overcome this difficulty and recover the coupling between completely de-mixed and localized (Frenkel) exciton states –which form the state space for the Frenkel Hamiltonian in Eq. 2 – we employed the aforementioned multi-state diabatization (MS-FED-FCF) (see Section 2.1).

The MS-FED-FCF diabatization procedure was carried out using 20 excited states of the supermolecular donor-acceptor system to ensure a complete de-mixing between excitations of different nature (e.g. charge transfer and other excitonic states) and an optimal reconstruction of localized Frenkel exciton states and related couplings. See convergence of V with the number of states in Figure 1 for the DCVSN5 system. At least 10 of the lower lying excited states are necessary to reach a converged value for V .²⁵

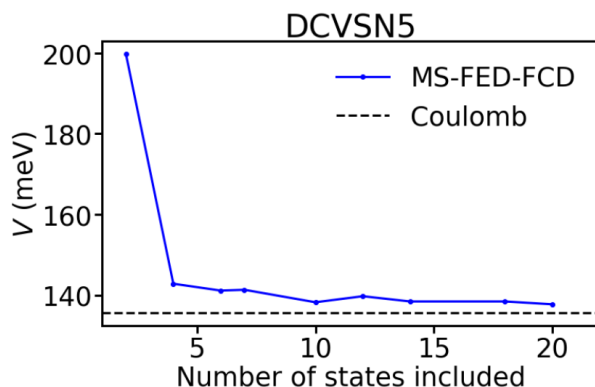


Figure 1: Convergence of the total V coupling as a function of the number of adiabatic states included in the MS-FED-FCF diabatization. Dashed black line indicates the V_{Coulomb} towards which V is converging pointing to a negligibly small short range contribution.

As a complementary analysis to Figure 2 in the main text, where there is an extremely good agreement between V obtained using a converged number of states in the diabatization procedure and both V_{Coulomb} and V_{TrESP} , in Figure 2 we report the same correlation but using only 2 states in the MS-FED-FCF (i.e. the regular FED). It is clear that the correlation is no longer optimal and the total excitonic coupling V between Frenkel exciton states includes unwanted mixing with excited states of different nature that yield, in most cases, an overestimated coupling value.

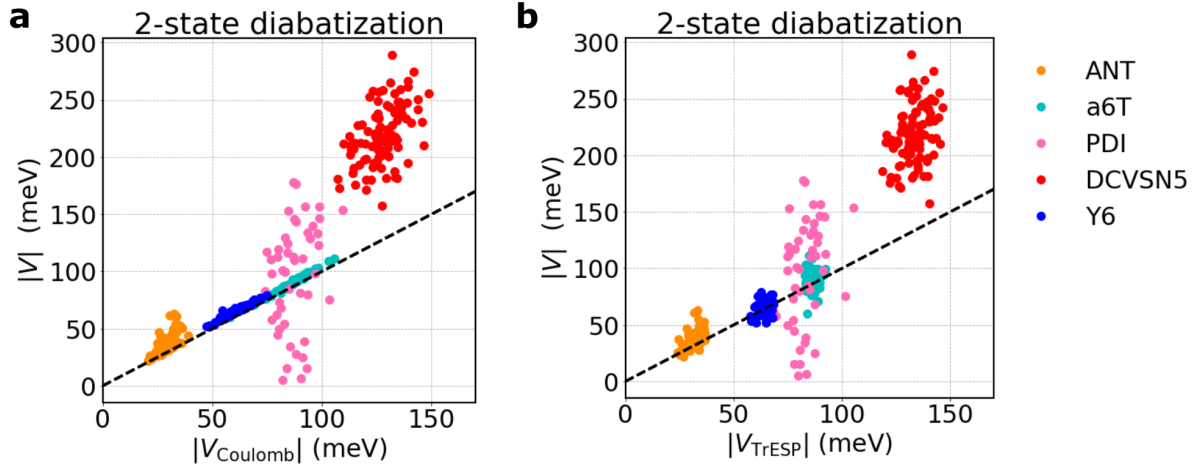


Figure 2: Correlation between the total excitonic coupling V , found using MS-FED-FCD with only 2 adiabatic states included in the diabatization procedure, and (a) V_{Coulomb} and (b) V_{TrESP} obtained for P_b , of ANT and a6T and P_a, P_{a1}, P_{a2} of PDI, DCVSN5 and Y6 respectively, extracted from MD trajectories of the various systems.

2.3 Excitonic coupling fluctuations

V_{TrESP} obtained by using the ESP fitting procedure described in the *Method* section is in very good agreement with V_{Coulomb} for all systems and crystal pairs investigated (see Table 1 in the main text). The notable difference is the fact that TrESP couplings are readily calculated without the need of repeating an electronic structure calculation for each different geometry. This constitutes a huge advantage of using TrESP approach in combination with FE-SH, as it permits calculating many thousands of coupling elements (and related nuclear gradients) at each step along the MD, thus allowing the study of large nano-scale systems. Additionally, this approach allows an efficient calculation of both couplings and coupling fluctuations beyond nearest neighbour pairs and to account for long-range interactions within the (Frenkel) Hamiltonian of these systems. These interactions are of vital importance to get a reliable estimate of the diffusion constant as it was recently pointed out in Ref.²⁶ and Ref.²⁷. The TrESP approach (combined with FE-SH) can help going beyond model Hamiltonians where only fixed nearest neighbour excitonic couplings are considered^{1,28}.

The TrESP method, although computationally very efficient, neglects any possible dependence of the transition density on the geometry. The time dependence of the excitonic coupling is solely related to the inverse distance dependence in Eq. 11 main text. To assess to which extent this is a good approximation and how well the TrESP approach can capture the fluctuations of the excitonic couplings, we computed both the Coulomb couplings and the TrESP couplings along 100 snapshots taken from an MD simulation (excitonic couplings for crystal pairs P_b , of ANT and a6T and P_a, P_{a1} of PDI, DCVSN5, respectively). The results are reported in Figure 3 along with related coupling distributions. To slightly refine the TrESP

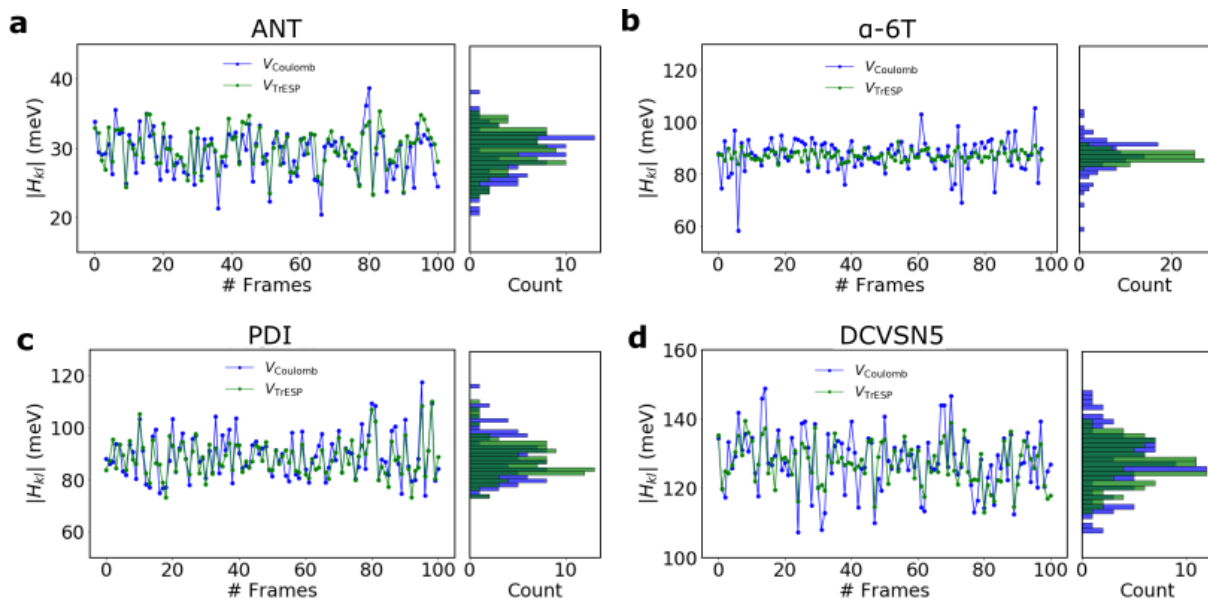


Figure 3: Excitonic coupling fluctuations for the investigated OSs. The couplings are evaluated (for P_b of ANT and a6T and P_a , P_{a1} of PDI and DCVSN5, respectively) with V_{TrESP} and V_{Coulomb} for a series of 100 MD snapshots. The distribution of these couplings are shown as well.

charges and partially account for more “exotic” configurations during the parametrization, we repeated the ESP fitting procedure for 50 different structures along MD simulations for each system and then averaged the TrESP charges over all configurations (instead of using just a single molecular structure). A sign-tracking procedure was adopted to keep consistent the sign of the charges when doing the average of TrESP charges.

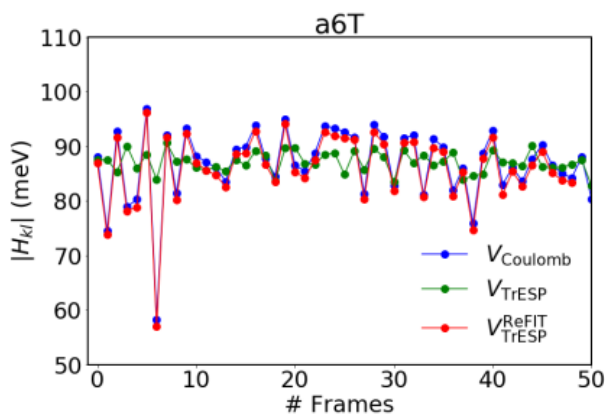


Figure 4: TrESP charges are re-fitted for different snapshots taken from an MD simulation of a6T (red line). The coupling V_{TrESP} is shown with a red line and compared with the TrESP coupling obtained by fixed pre-parametrized charges (green line) and the reference V_{Coulomb} (blue line)

We can observe that for all the systems the TrESP approach is able to capture the mean value of the coupling extremely well. Interestingly, the coupling fluctuations and the structural dependence of the

excitonic couplings are reasonably well captured for ANT, PDI and DCVSN5 as well. While, in a6T, the TrESP coupling fluctuations are somewhat underestimated compared to the V_{Coulomb} . The explanation for this behaviour is simply that for the first three molecules (ANT, PDI and DCVSN5) the rigidity of the aromatic structure and extended conjugation ensure that the transition density does not change significantly along the dynamics. Thus, TrESP charges provide a reasonable approximation for the latter. On the contrary, having a more flexible structure, a6T shows larger structural variations along MD. A similar conclusion holds for Y6 as well. In this case, the TrESP approach does not capture as well the dependence of the transition density on the geometry. However, excitonic coupling fluctuations (as found using electronic structure) are small compared to the actual mean coupling in a6T (i.e. only about 5% compared to the excitonic coupling). Thus, even though the TrESP approach cannot completely capture their magnitude, this is not expected to make any consistent difference for the calculation of transport properties.

We conclude by remarking that, despite the TrESP approximation inevitably leads to a small loss of accuracy if compared with the rigorous Coulomb integral calculation especially for flexible molecules (e.g. polymers), it provides a very efficient scheme to evaluate a large number of coupling matrix elements along MD dynamics. It is also very accurate when it comes to mean couplings and fluctuations of rigid conjugated molecules. Updating the transition charges along the MD could help in further increasing the accuracy of TrESP charges even for difficult cases. This could be achieved, for example, using, more sophisticated interpolation schemes (e.g. machine-learning techniques²⁹). See for example Figure 4, where the TrESP charges were re-fitted for different geometries. In this case, a perfect agreement is re-established between the V_{Coulomb} and $V_{\text{TrESP}}^{\text{ReOPT}}$.

2.4 Point dipole approximation

As it is customary in Förster theory, at sufficiently large distances between sites (i.e. distance larger than the dimension of the interacting molecules), the transition densities of donor and acceptor can be approximated with the first non-zero term in a multipole expansion, i.e. the transition dipole moment. This approximation is referred to as point dipole approximation (PDA) and the related excitonic coupling, V_{PDA} , can be written as,

$$V_{kl}^{\text{PDA}} = \frac{\mu_k \cdot \mu_l}{r_{kl}^3} - \frac{3(\mu_k \cdot \mathbf{r}_{kl})(\mu_l \cdot \mathbf{r}_{kl})}{r_{kl}^5} \quad (8)$$

where \mathbf{r}_{kl} is the vector distance between k and l molecules and μ_k and μ_l their respective transition dipole moments. We found that the PDA approximation breaks down for all molecules except ANT and should not be used (see Section 2.5).

2.5 Distance dependence of excitonic couplings

In order to explore the distance dependence and the long-range nature of the excitonic couplings, and to find how well the observations made before for the closest crystal pairs can be generalized to molecules further apart, we performed coupling calculations displacing the the two molecules forming the π -stacked pairs (P_b , of ANT and a6T and P_a , P_{a1} of PDI, DCVSN5, respectively) at various distances. The results are reported in Figure 5 for some of the systems analysed in this work.

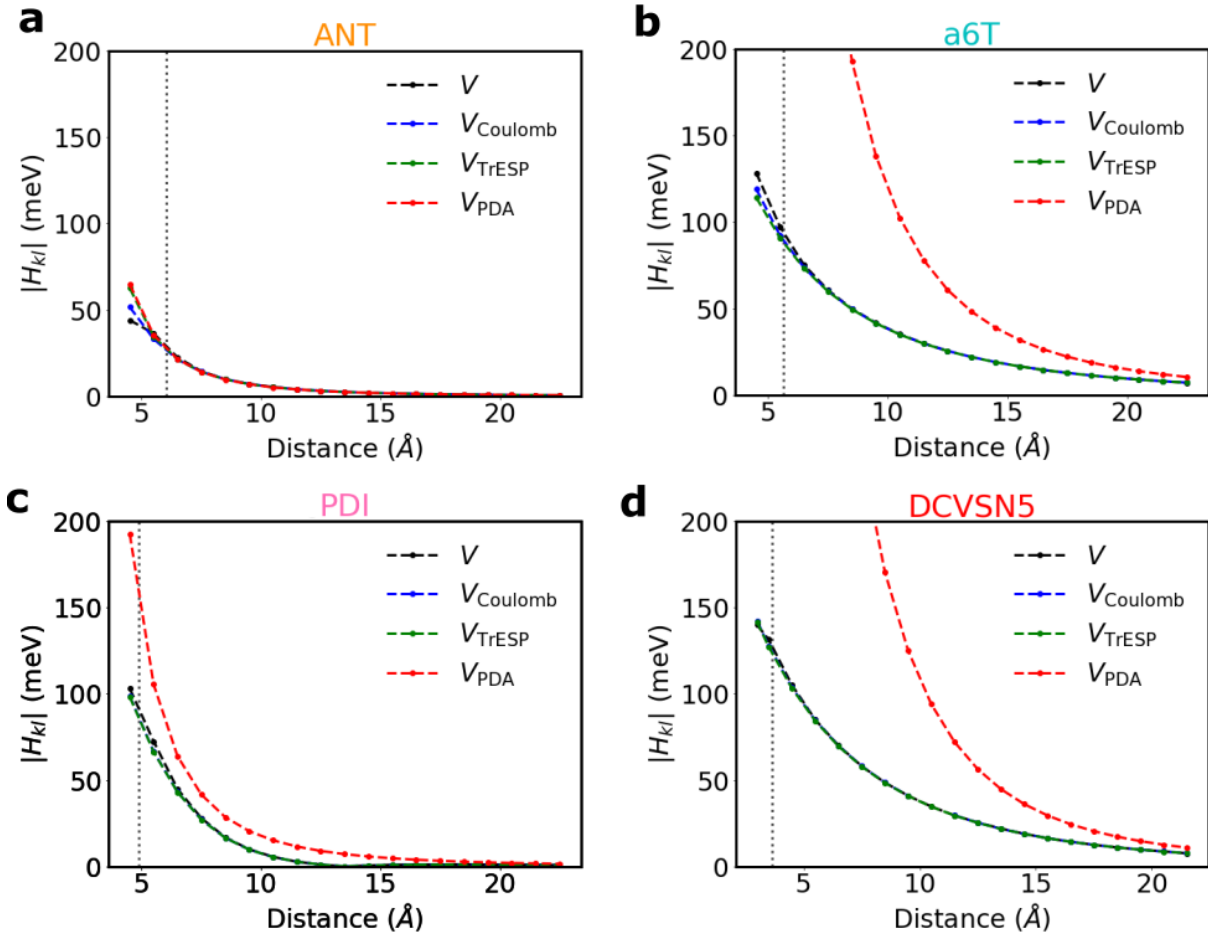


Figure 5: Excitonic couplings as a function of distance for the pairs of ANT, a6T, PTCDI-H and DCVSN5 mentioned in the text. Couplings are given in absolute values and have been evaluated using MS-FED-FCD diabatization approach (using the first 20 excited states for the diabatization procedure), V_{Coulomb} (Eq. 10 main text), V_{TrESP} (Eq. 11 main text) and V_{PDA} (Eq. 8). The PDA clearly fails to provide an accurate description of the excitonic coupling at short intermolecular distances.

As expected, V , V_{Coulomb} , V_{PDA} and V_{TrESP} , all perform very similarly at large distances, that is when the higher multiple terms of the transition densities can indeed be neglected. We note that the total excitonic coupling, V , becomes quite small beyond 20 Å in all systems. Notably, as the distance decreases, and the closest distance between molecules in the crystal is approached (vertical dashed black line), the

V_{PDA} approximation (red line) diverges from the other solid lines leading to strongly overestimated couplings for all the systems, but ANT. The reason is that the PDI molecule and, in particular, a6T and DCVSN5 have spatially extended transition densities and, when the distance between the sites falls below the actual spatial extent of the electronic transition density, the PDA breaks down and it should no longer be used (i.e. the actual shape of the transition density needs to be taken into account). This suggests caution in the application of Förster theory when describing exciton dynamics for molecular semiconductors composed of medium-sized and large organic molecules. On the opposite, the V_{TrESP} (green line) gives very good coupling estimates within the full distance regime, proving again to be a useful method.

As a final observation, we note that, for all the systems investigated here, short range effects, V_{Short} , remain negligible even below the shortest crystal pair distance (dashed black vertical line), and the V_{Coulomb} is still a reasonably good approximation of the total V . Yet, short range effects might become important at even shorter distances when the overlap between donor acceptor wavefunctions becomes larger.

2.6 Transition dipoles

In Figure 6 we show the transition dipoles obtained using TrESP charges.

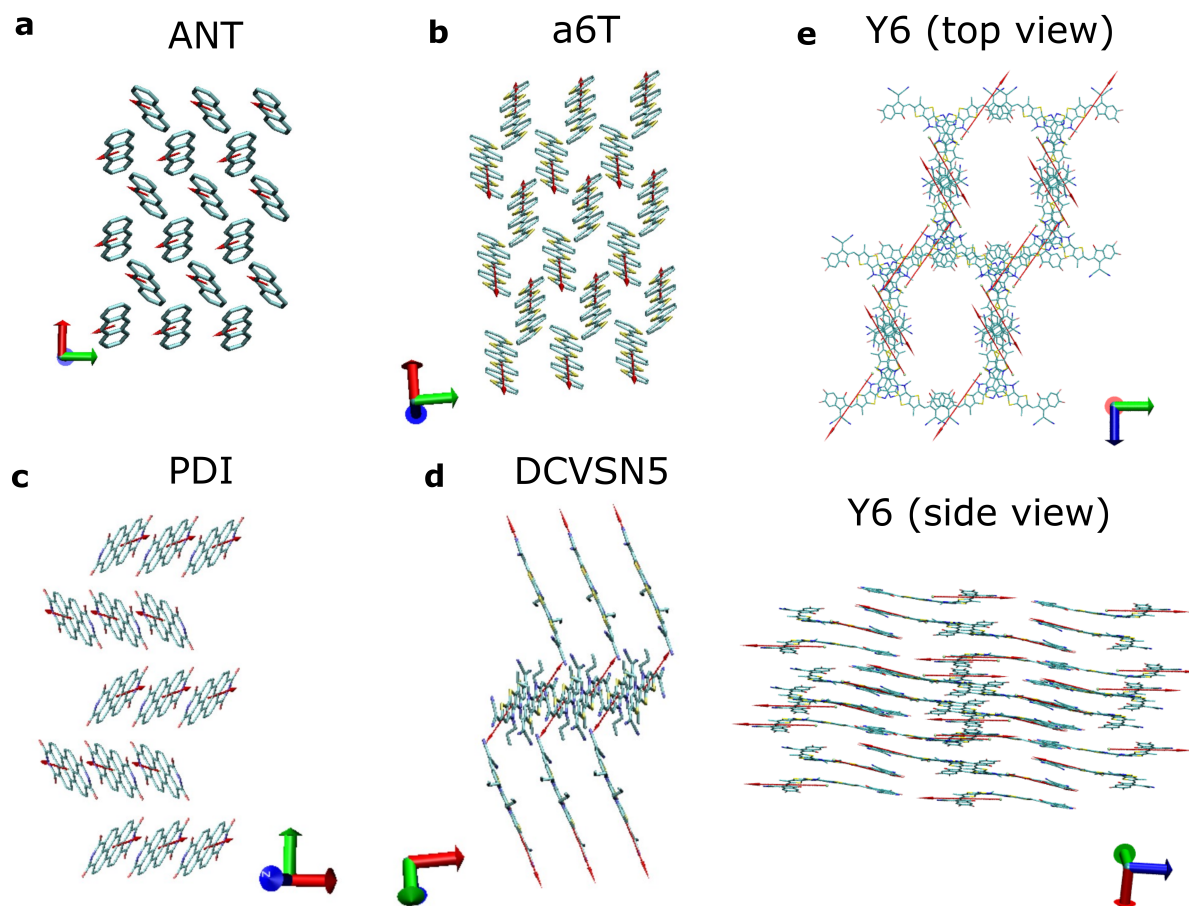


Figure 6: Transition dipoles (obtained from TrESP charges) depicted on each molecule of the systems investigated.

3 Exciton diffusion dynamics and simulation details

3.1 Cell parameters

Table 2: Unit cell parameters (Å), transport direction investigated and related super cell information.

System	ANT	a6T	PDI	DCVSN5	Y6
a	8.562	9.140	4.865	7.341	14.469
b	6.038	5.684	14.660	27.685	21.186
c	11.184	20.672	10.844	12.527	30.842
α	90.000	90.000	90.000	90.000	109.352
β	124.700	97.780	91.330	103.828	96.264
γ	90.000	90.000	90.000	90.000	98.409
Z	2	2	2	4	4
Dir.	$a - b$	$a - b$	$a - b$	a	a
Super cells	12x16x2	16x16x2	24x12x2	54x2x2	48x2x1
Tot. atoms	18432	45056	46080	45792	32640

3.2 Force-field parametrization

The force field parameters for calculation of the site energies of the Hamiltonian Eq. 2 (in the main text), H_{kk} , are parametrized to reproduce the intramolecular exciton reorganization energy from TD-DFT calculations as reported in Table 1. In particular, the force field equilibrium bond lengths of the excited state, $\mathbf{R}_{Ex,k}$, is adjusted by scaling the DFT displacements, $\Delta\mathbf{R}_k^{\text{DFT}}$, namely: $\mathbf{R}_{Ex,k} = \mathbf{R}_{N,k} + \beta\Delta\mathbf{R}_k^{\text{DFT}}$, until force field and TD-DFT reorganization energies (Eq. 12 in the main text) match. When the scaling constant β is close to unity this means that the displacements in the force field and in TD-DFT are almost identical. All other intra- and inter-molecular parameters were chosen to be the same as for the ground state. In Figure 7, we report the displacement found by electronic structure for the ground and first excited state of the different organic molecules considered in this work.

The site energies H_{kk} of the Hamiltonian and their nuclear gradients $\nabla_I H_{kk}$ are obtained by assigning molecule k the force field parameters for the excited state and all other molecules $l \neq k$ the parameters for the ground state as previously done for the fragment orbital-based surface hopping (FOB-SH) in the context of charge transport.³⁰⁻³² In the case of Y6, alkyl side-chains were removed from the simulation for simplicity and replaced by center of mass positional restrains of $1.255 \text{ Kcal mol}^{-1} \text{ \AA}^{-2}$ force constant to keep the structure close to the crystalline packing arrangement (RMSD 1.768 Å).

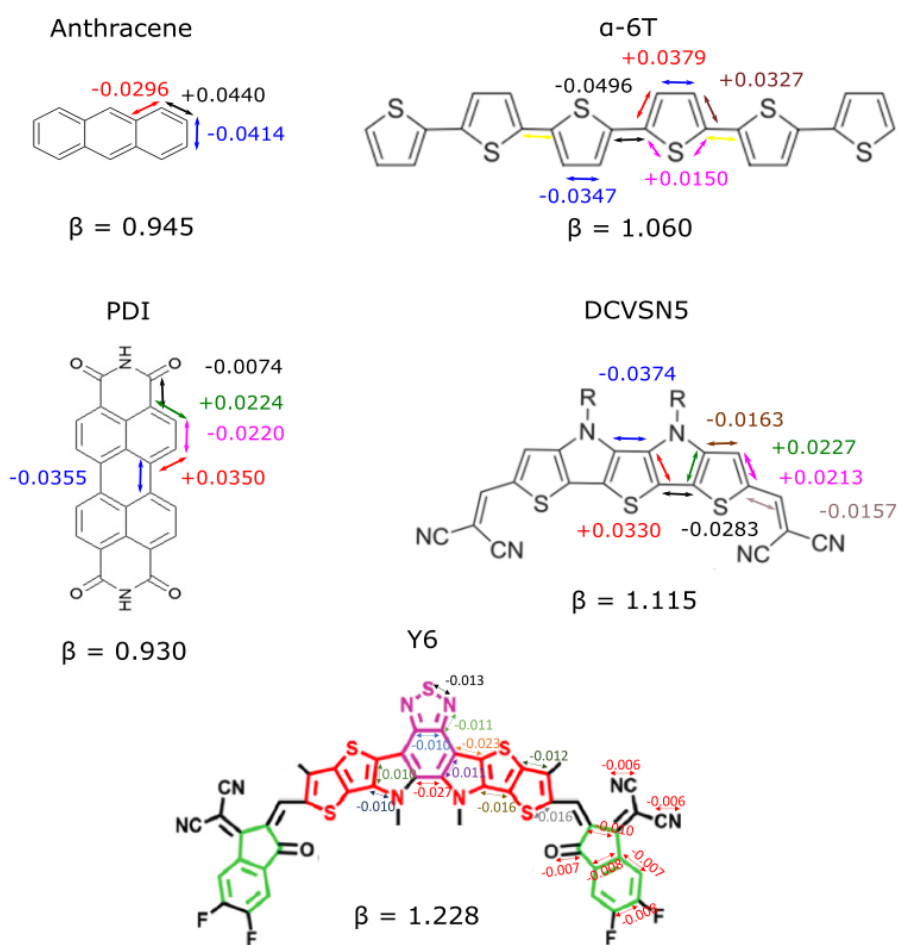


Figure 7: Force field parametrization for singlet excitons. Changes in bond length upon change from ground to excitonic state, as obtained from TD-DFT calculations. Displaced bond distances in Å are reported with different colours according to the displaced bonds. The + and – signs indicate an increase and decrease in bond length going from the ground to the excited system, respectively. The displacements are used to parametrize the force field for the molecules in their lowest energy singlet state. For clarity, displacements symmetric to the ones indicated are not shown. The scaling factor β for force field parametrization according to the TD-DFT reorganization energy, as described in the text, is also reported for each system.

3.3 Convergence exciton diffusion constants

Simulation details are given in *Methods* section of the main text.

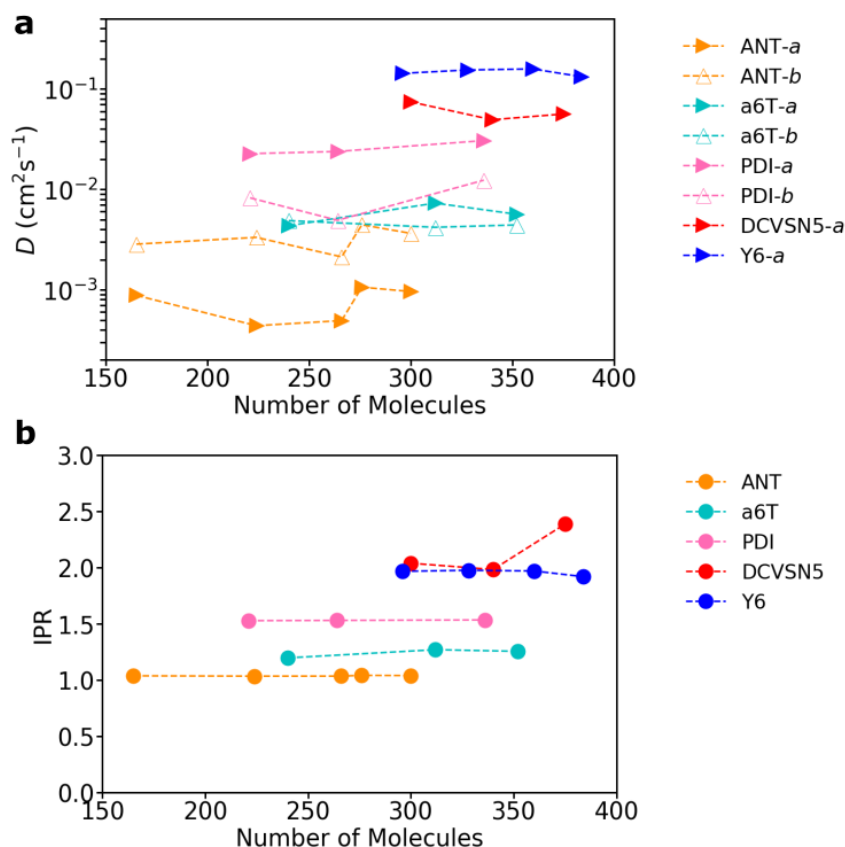


Figure 8: (a) Convergence of the diffusion constant as a function of the number of electronically active molecules. The diffusion constant is obtained from linear fits to the MSD after initial relaxation, as described in the main text. (b) Convergence of the IPR as a function of the number of active molecules. The time step used for FE-SH simulations was set to 0.01 fs for all the system in order to tackle as well as possible the trivial crossing issue.

3.4 An assessment of different methods: the case of anthracene

Anthracene represents a useful system to benchmark the FE-SH as the diffusion constant and related diffusion length have been evaluated by other authors using of Marcus-like rate expressions¹ as well as Boltzmann-corrected Ehrenfest dynamics³³. Some experimental estimates of the diffusion constant, that can be used as a suitable reference, are also available³⁴⁻³⁶. As seen in Table 1, the reorganization energy of ANT is quite high compared to the excitonic coupling, supporting the formation of excitons mostly localized on a single molecule. The IPR calculated from FE-SH simulations, Eq. 8 (main text), is on average 1.04. This small IPR can be readily explained by considering that the barrier for exciton hopping between different molecules (estimated with Eq. 1) is about 112 meV which is much higher than the largest coupling in the crystal of around 30 meV and the thermal energy at room temperature (25 meV). This observation has justified the use of perturbative rate theories¹ to study the transition mechanism for this system (see below). Notably, as shown in Figure 3 and already observed in the literature¹, the

exciton couplings in anthracene exhibit sizeable thermal fluctuations compared to the mean coupling which provides a good motivation to explore direct dynamics methods (such as FE-SH and Ehrenfest) as well.

To assess the quality of FE-SH simulations we report in Table 3 a comparison between the diffusion constants and related diffusion lengths (estimated using an exciton lifetime of $\tau = 10$ ns as found by experiments³⁴) with the same values obtained from different computational methods and available experimental estimates. In particular, to calculate the diffusion constants, Elstner’s group in Ref.³³ employed semi-empirical time-dependent density functional tight-binding (TD-DFTB) method in combination with Ehrenfest dynamics. The latter approach was opportunely corrected to approximately satisfy detailed balance (which is very important for an accurate dynamics as detailed in Ref.²⁷). This approach is referred to as Boltzmann-corrected Ehrenfest method (BC-Ehrenfest). Using transition densities taken from TD-DFTB, the authors obtained averaged Coulomb couplings along MD ($\sqrt{\langle |H_{kl}|^2 \rangle}$) of about 31 meV for P_b and 11 meV along T pairs. These values are very similar to what found in this work from the TrESP approach ($\sqrt{\langle |H_{kl}|^2 \rangle}$) about 30 meV and 7 meV for P_b and T pairs, respectively). However a smaller reorganization energies of 302 meV was found in the former work, as a consequence of the approximate DFTB approach that relies on local functionals to describe the excited state geometry. This reorganization energy was employed to model the exciton-phonon coupling leading to a weaker exciton relaxation compared to TDDFT used in FE-SH, where the exciton reorganization energy is 561 meV. It also is worth pointing out that the DFTB implementation is more expensive than the FE-SH methodology coupled to an effective Hamiltonian proposed in this work. For this reason, in Ref.³³, 1D chains were considered. As shown in Ref.³¹, the reduced dimensionality could have a sizeable impact on electronic transport properties such as wavefunction delocalization and diffusion constant. Nevertheless, despite all these differences and the different underlying dynamics, FE-SH and BC-Ehrenfest methods yield similar diffusion constants (see Table 3). The diffusion lengths from FE-SH and BC-Ehrenfest are both slightly underestimated compared to the experiments (see main text for a discussion on this point).

In Table 3 we also compare both numerical non-adiabatic propagation schemes with the perturbative rate theory used in Ref.¹ by Arag3 et. al as well. The latter approach is reasonably well justified in this system by the high local exciton-phonon coupling and the incoherent hopping mechanism (observed by inspecting non-perturbative FE-SH trajectories, see e.g. Figure 3 main text). The rate expression used in Ref.¹ is very similar to the Marcus-Levich-Jortner rate for electron transfer^{24,37}. It introduces an effective quantum high-frequency mode that is coupled to the exciton transfer process in order to effectively account for quantum-mechanical vibrations. In fact, in the common Marcus expression all vibrational modes in the system are treated as classical harmonic oscillators. While such an approximation is generally good for treating low frequency motions of a general solvent, it is not completely accurate for intramolecular modes of the molecules, since for these modes $\hbar\omega > k_B T$. The approach employed by Arag3

Table 3: Couplings (meV) for P_b pair, diffusion constants and diffusion lengths from different computational methods and experiments.^a

	FE-SH ^b	BC-Ehrenfest ^c	MLJ-Rate ^d	Exp. ^e
$\sqrt{\langle H_{kl} ^2 \rangle}$ ^f (meV)	29.6	30.5	35.9	-
λ^{XT} (meV)	561	302 ^g	589 ^h	-
D_a (cm ² s ⁻¹)	7.7E-04	7.1E-04	2.9E-03	1.8E-03
D_b (cm ² s ⁻¹)	3.3E-03	2.4E-03	8.2E-03	5.0E-03
L_a (nm)	39	38	76	60
L_b (nm)	81	69	128	100

^a The diffusion length is estimated as described in the main text for all the different methodologies using an exciton lifetime $\tau = 10$ ns, as obtained by experiments³⁴. ^b FE-SH simulations are performed as described in *Methods*. ^c Boltzmann corrected Ehrenfest values are taken from Ref.³³. The authors used reduced dimensionality 1D models along a and b crystallographic directions. ^d Perturbative rate theory result are taken from Ref.¹. A rate expression very similar to the Marcus-Levich-Jortner rate for electron transfer was used by the authors by including an effective quantum mode coupled to the excitation energy transfer process. ^e Experimental estimated for the diffusion lengths are taken from Ref.^{35,36}. ^f Excitonic couplings (averaged along MD trajectories) are given for P_b in the crystal. ^g Reorganization energy from TDDFTB ^h Reorganization energy obtained using normal mode analysis based on Huang-Rhys factors evaluation and the same level of theory as for FE-SH.

et al. gives a diffusion constant in the same order of magnitude as FE-SH and BC-Ehrenfest approaches and slightly longer diffusion length compared to both non-adiabatic propagation schemes. This can be explained with the fact that high frequency vibrations play a non-negligible role for the transport and, for systems with a reasonably high activation barrier (e.g. ANT), a classical treatment of modes might not be entirely justified (even at room temperature). This fact provides an additional explanation for the lower diffusivity predicted by the FE-SH and BC-Ehrenfest approaches, which treat all the modes with classical force fields, compared to both experiment and Marcus-Levich-Jortner like expression. On the other hand, the excitonic couplings computed in Ref.¹ were found by using a diabaticization scheme that, to the best of our understanding, includes only 2 adiabatic states¹. Therefore the coupling between Frenkel exciton states is possibly an effective coupling still contaminated by mixing with charge-transfer states. For this reason, these couplings are slightly larger compared with both TrESP and TD-DFTB couplings (which by constructions do not include such a mixing with charge transfer states).

Overall, considering the differences in simulation set-ups, parameters entering the various Hamiltonians or analytic expressions and the uncertainty commonly characterizing experimental measurements, we show in Table 3 that the agreement between FE-SH and other literature data is very encouraging.

3.5 Comparison between diffusion from FE-SH and the literature

By comparing a6T and ANT systems, that have a comparable exciton reorganization energy (see Table 1), one can see a larger MSD in a6T crystal compared to ANT and a factor of 2 larger diffusion in the former system when considering the high diffusion directions of both OSs (i.e. b direction for ANT, for which

FE-SH yields $D_b = 3.3 \times 10^{-3} \text{ cm}^2 \text{ s}^{-1}$, and a direction for a6T for which we found $D_a = 5.8 \times 10^{-3} \text{ cm}^2 \text{ s}^{-1}$). This is a direct consequence of the larger excitonic coupling in a6T compared to ANT.

These numbers compared quite nicely with our simulations, although it is fair to point out that the measured diffusion constant for a6T system does not refer to the crystal structure (studied herein), but it is rather characteristics of a thin-film of a6T molecules vacuum-deposited on quartz. Different structures and morphologies of the sample make difficult a like-for-like comparison between FE-SH simulations and experiments and this should be taken just as indicative. The exciton diffusion length of this system was reported to be about 60 nm by the quenching of the photoluminescence. In our estimates of the experimental diffusion constant we assumed 2D diffusion within the herringbone layer characterizing this system.³⁸

In contrast to both a6T and ANT, despite having a larger diffusion constant (as found from FE-SH simulations) of about $D_a = 26 \times 10^{-3} \text{ cm}^2 \text{ s}^{-1}$, PDI has a diffusion length of less than 1 nm due to the fast decay of the exciton to the ground state (of about 100 fs³⁹). A negligible diffusion length was also found in Ref.³⁹ for a thin-film PDI derivative with a linear butyl side-chain, although, once again the comparison can only be indicative.

The comparison between the experimental estimates of diffusion constant and diffusion length of Y6 and FE-SH should also be taken as indicative. In fact, Y6 has a thin-film morphology. In order to measure the exciton diffusion length, Ref.⁴⁰ measures the exciton-exciton annihilation rate γ and calculate the exciton diffusion coefficient D according to $\gamma = 4\pi DR_0$. The above equation can be derived through solving the 3D diffusion equation. In the deduction, the 3 dimensionality is embodied in the factor of 4π . In general the diffusion length is dependent on the system dimension and it can be defined $L = \sqrt{nD\tau}$. Where $n = 2, 4, 6$ for 1D, 2D and 3D diffusion respectively. Experimentally however, in Ref.⁴⁰. L is defined as $L = \sqrt{D\tau}$. Therefore in Table 2 of the main text we provided values from both definitions of the diffusion length applied to a 3D model.

3.6 Delocalization of thermally accessible states as a function of interactions range

It has been recently reported that the long-range excitonic interactions can drastically modify the exciton diffusion constant in ordered nanofibers of P3HT depending on the length of the polymeric fibers.^{26,27} Prodhan and co-workers²⁷ found that the diffusion constant increases dramatically in long polymer chains when long-range interactions are included in the description. On the opposite, it was found that the same long-range interactions are responsible for a smaller value of the diffusion constant in shorter polymer chains (e.g. with 6 thiophene units).

In the present FE-SH simulations on the molecular semiconductors analysed in this work the full-range

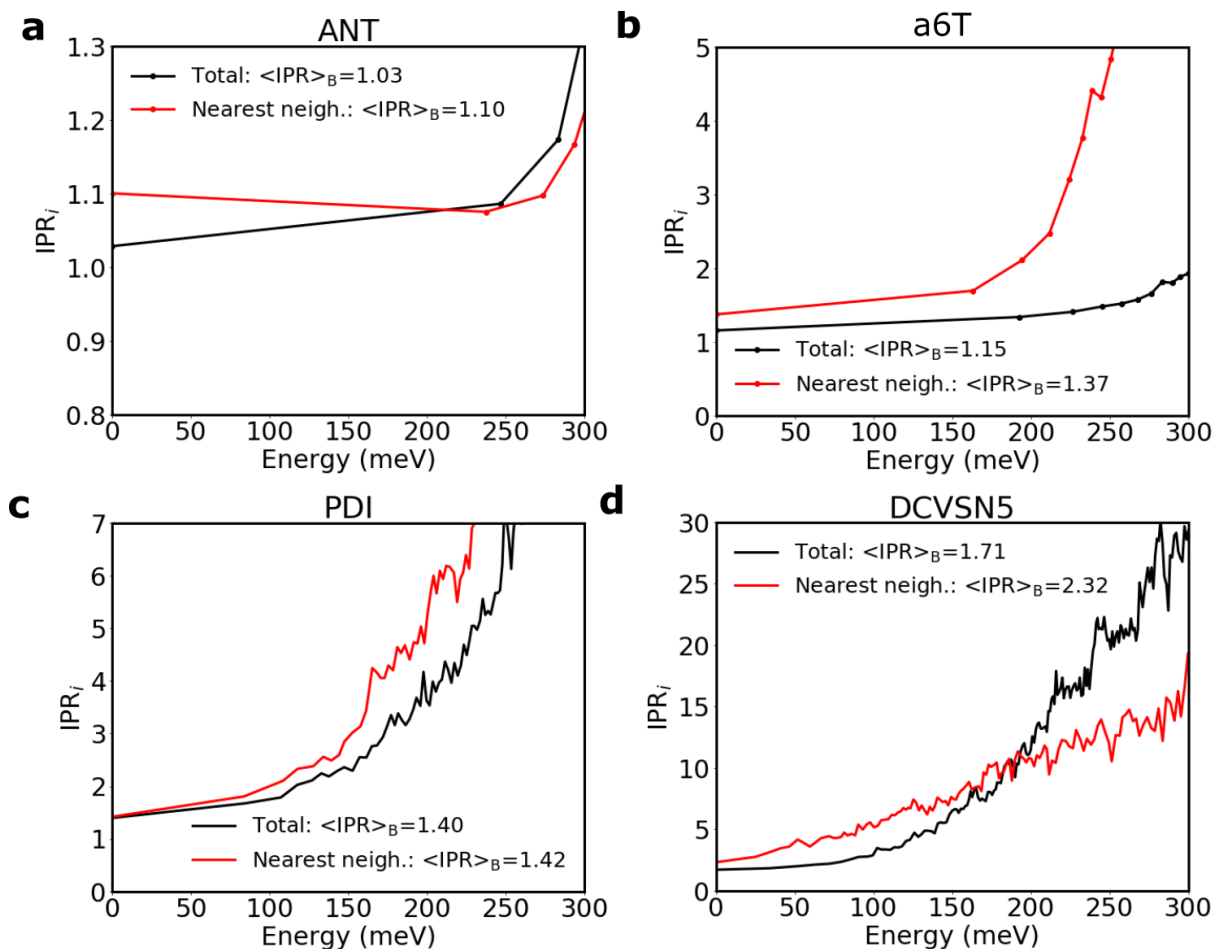


Figure 9: Effect of removing long-range interaction on the delocalization of the states at the bottom of the excitonic band. The IPR_i (Eq. 9 main text) of the adiabatic states is plotted against their energy in red when only nearest neighbours are retained and black when the full interaction range is considered. Note how the thermally accessible states below 200 meV are generally slightly more delocalized when only nearest neighbour interactions are considered.

of interactions is considered in order to obtain the most accurate description possible for the diffusion constant. It is interesting, however, to investigate the role of long-range interactions in the molecular systems presented here as a complement to the polymeric chains investigated in Ref.²⁶ and Ref.²⁷. To estimate the impact that removing the long-range interactions has on the delocalization of the thermally accessible states of the excitonic band (and therefore on the diffusion constant), in Figure 9 we plot the IPR of the states as a function of their energy (Eq. 9 main text), both when the full range of interactions is considered (black line) and when only nearest neighbours are retained (red line). Interestingly, we observe that in the latter case, the lower energy tail states become slightly more delocalized compared to the case where the full range of excitonic interactions is considered (note that this is no longer the case for the states in the middle of the excitonic band which are always more delocalized when long-range

interactions are considered for the systems investigated). This increase in the extent of delocalization of the excited states can be quantified Boltzmann weighting the IPR_i (Eq. 9 main text). This value is larger when only nearest-neighbour interactions are retained in the Frenkel Hamiltonian. Thus, we expect long-range interaction to be indeed slightly detrimental for the exciton transport and diffusion constant in all these molecular systems (as it was found in short polymer chains²⁷).

As additional verification of the (small) detrimental effect of long-range interactions on the exciton diffusion properties of these systems, we show in Figure 10 that for a single chain of DCVSN5 the exciton extends over more sites when only nearest-neighbour interactions are considered. This observation acts as an additional explanation of why charge carrier (which are naturally subjected to short-range interactions) delocalize more than excitons in these molecular crystals.

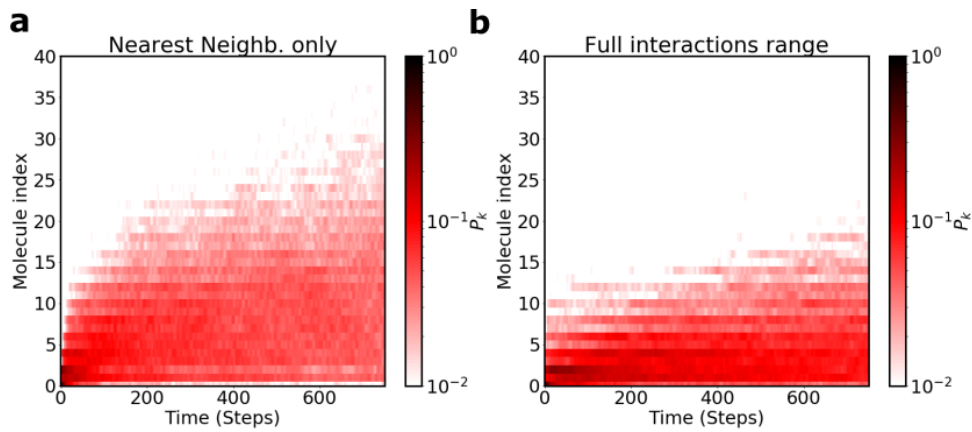


Figure 10: Sum of 600 individual surface hopping simulations of exciton diffusion in a single chain of DCVSN5 with and without long-range exciton couplings. Note how the exciton populates many more molecules when long-range interactions are removed and only nearest neighbour interactions are retained.

4 Comparison charge vs exciton

4.1 Transport parameters

In Table 4 we compare transport parameters characterizing hole and exciton transport for some of the organic crystals investigated in this work. We report hole transfer interactions for the same crystal pairs in Figure 1 (main text) and hole reorganization energies and compared these with excitonic interactions (V) found using MS-FED-FCD and related reorganization energies.

The hole transfer couplings have been computed using two different approaches. On the one hand, we used the well-established fragment orbital density functional theory (FODFT) approach Ref.^{30,31,41}. This method is related to the interaction between the diabatic state wavefunctions constructed from orbitals of the isolated donor and acceptor fragments (similarly to what happens in constraint density function theory (CDFT), but unlike in CDFT, the interaction between donor and acceptor fragments is neglected). FODFT calculations are carried out with the CPMD program package using the PBE exchange correlation functional as previously done in Ref^{30,31,41}. We also used a projection operator-based diabatization (POD) approach as Ref.^{42,43}, as a further way of computing charge transfer couplings. This approach is a diabatization scheme based on the self-consistent DFT Kohn-Sham Hamiltonian of the donor-acceptor system in question, represented in an orthogonalised atomic orbital basis and partitioned into donor and acceptor blocks. Each block is separately diagonalised, defining unitary transformations which are used to transform the off-diagonal blocks. The resulting off-diagonal matrix elements may be identified as electronic couplings between the block-diagonal donor and acceptor states. The Kohn-Sham DFT calculations were carried out with the PBE functional, a DZVP basis set and GTH pseudopotentials on the neutral dimer (using CP2K program package). After block diagonalization, the Hamiltonian matrix element between the HOMO POD states on each molecule is taken as the electronic coupling matrix element. Both FODFT and POD couplings are scaled by a factor 1.3 (giving sFODFT and sPOD) for the best agreement with high-quality ab-initio coupling estimates as done in Ref.^{41,42}.

The first important observation is that, despite being very different approaches, FODFT and POD yield very similar coupling values for all the systems considered. Hole transfer couplings are comparable in magnitude to the corresponding excitonic couplings (obtained with MS-FED-FCD as described in Section 2.1), although slightly smaller especially in the case of a6T. Hole transfer couplings are also less isotropic compared to excitonic interactions. Another notable observation is that generally, the excitonic couplings fluctuations are smaller than the corresponding fluctuations of charge transfer couplings in the case of charge transport. It has been pointed out before³¹ that the coupling fluctuations actually enhance the delocalization of the states and help the transport in the hopping regime (while they become detrimental in the band-like regimes as they act as scattering sites). This observation give an additional explanation for the fact that exciton transport in the investigated systems (where there is a reasonably

Table 4: Couplings (in absolute values) and reorganization energies for hole and exciton transport for the investigated systems. FODFT and POD couplings were scaled by 1.3.^{41,42} MS-FED-FCD couplings include 20 states in the diabaticization procedure. Hole reorganization energies employ 6-31G(d,p) basis-set (consistently with the one used for the corresponding exciton reorganization energy). All values in meV.

		Dist (Å)	Hole (meV)			Exciton (meV)	
			sFODFT	sPOD	λ^h	MS-FED-FCD	λ^{XT}
ANT	P_b	6.04	56.99	53.20	137.8	27.88	560.7
	T	5.24	25.22	23.93		6.40	
	P_a	8.56	0.16	0.28		4.35	
a6T	P_b	5.68	4.78	1.17	253.7	91.92	558.1
	T	5.38	47.35	46.39		101.15	
	P_a	9.14	0.21	0.23		42.01	
PDI	P_a	4.87	109.94	110.80	152.5	100.06	390.5
	T_1	9.47	0.38	0.42		31.97	
	T_2	9.40	0.95	0.89		17.89	
	T_3	11.60	1.61	1.39		14.01	
DCVSN5	P_{a1}	3.64	161.95	161.57	155.0	137.65	320.1
	P_{a2}	4.46	181.77	188.31		151.93	
	T_1	14.2	0.36	0.08		24.14	
	T_2	14.81	1.45	1.09		23.65	

high barrier) is slower than the corresponding charge transport (see Figure 5 in the main text).

The most important difference between hole and exciton is the magnitude of charge reorganization energies as compared to the corresponding exciton reorganization energies. Taking as an example the anthracene molecule (see Figure 11), the hole reorganization energy is ≈ 140 meV while the relaxation of the exciton is about four times larger. This is due to the large charge redistribution occurring upon excitation. In particular, just by looking at the NTOs, it is evident that almost every bonding interaction in the HOMO becomes an anti-bonding interaction in the LUMO and vice versa. This causes each bond to become stronger (in case of a bonding interaction) or weaker (for an anti-bonding one) changing the length of the actual bond and causing a large structural modification upon excitation (see also Figure 11). These sizeable reorganization energies, that in FE-SH are used to re-parametrize the classical FF as explained in the main text, are responsible for the strong exciton localization in these systems. Bond lengths displacement used for the parametrization of the force field of the excitonic state are reported in Figure 7.

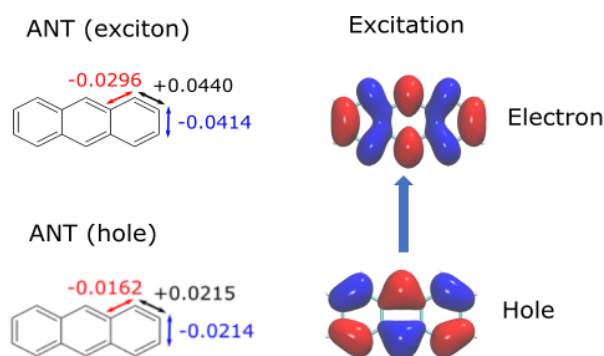


Figure 11: Bond displacement for exciton and charge states. The + and – signs indicate an increase and decrease in bond length going from the ground (neutral) to the excited (charged) system for exciton (charge), respectively. The displacements are used to parametrize the force field for the molecules in FE-SH and FOB-SH respectively. The NTOs related to the excitation of ANT are also shown.

4.2 Charge vs exciton transport mechanism

Having previously analysed both charge and exciton transport parameters, we show in Figure 12 a representative surface hopping trajectory for both transport cases within the herringbone plane of the anthracene crystal. The most striking difference is related to the transport mechanism of charge and energy carriers. Indeed, while the excitonic wavefunction is completely localized on a single molecule and it is hopping from one molecule to a neighbouring one, the corresponding charge carrier wavefunction is much more delocalized ($\text{IPR} \approx 5$) and it is characterized by a extended diffusive jumps as described in Ref.³¹ for other high mobility organic crystal. The thermally accessible valence band states are more delocalized in ANT than the corresponding excitonic states, and this allows the charge carrier wavefunction to extend to several molecules (more than 15 in the example trajectory of Figure 12) and to cover a longer spatial displacement compared to the localized exciton. This is a consequence of the more efficient transient delocalization. As we already showed in Figure 3 in the main text, a larger wavefunction delocalization correlates with a faster transport and a larger diffusion constant. In the particular case of ANT, the diffusion constant is much larger in the case of hole transport than to the corresponding exciton diffusion constant ($D=0.0905$ vs 0.0033 , respectively, along b direction of ANT crystal).

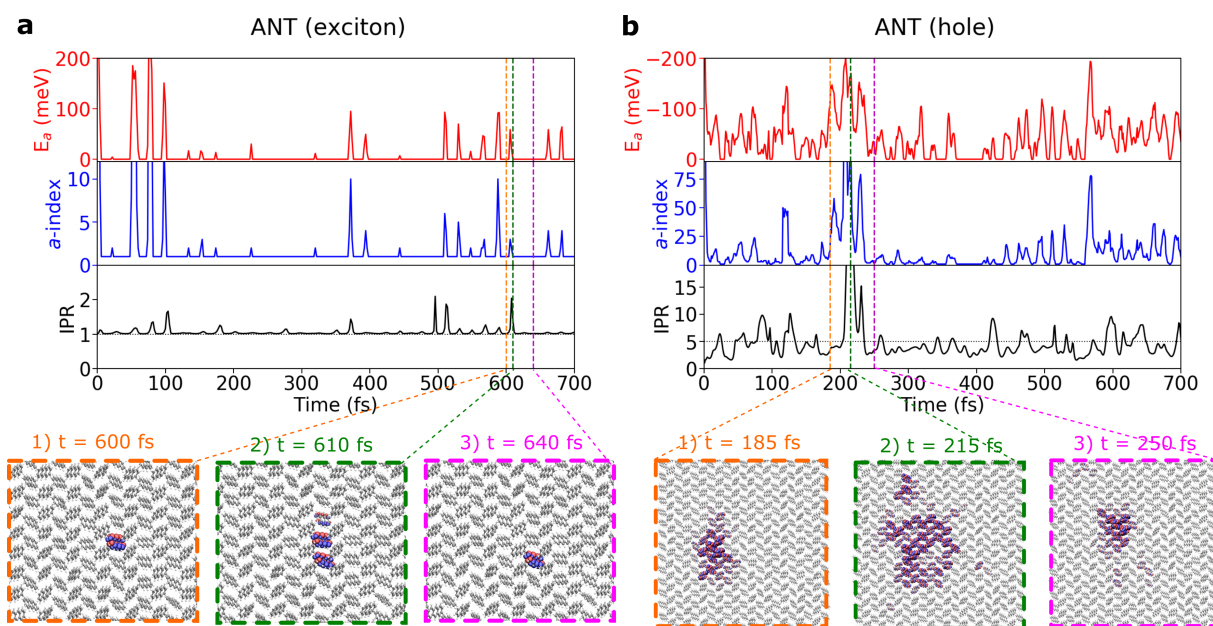


Figure 12: Transient delocalization mechanism of exciton and charge carriers in ANT: Panels (a) and (b), respectively. Both panels show time series along a single representative FE-SH trajectory for ANT-exciton performed with FE-SH and for ANT-hole performed with FOB-SH. Top panels: energy of the active potential energy surface on which the nuclear dynamics is taking place in our simulations, E_a (red lines). Middle panels: index of the active exciton band state, a (blue lines, index $a = 0$ corresponds to the ground state which is at the bottom of the excitonic band). Bottom panels: IPR of the exciton and charge carrier wavefunctions in the two cases respectively, $\Psi(t)$ (black lines) and average IPR of $\Psi(t)$ over the swarm of surface hopping trajectories (horizontal dashed grey lines). Note the correlation between the intra-band excitations, i.e. eigenstate index a , excitation energy and IPR of $\Psi(t)$. Additional panels below (a) and (b) depict a representative “transient delocalization event” of the both exciton and charge wavefunctions resulting in wavefunction displacement and diffusion. Initially the exciton is localized over one molecule, while the charge forms a larger polaron in ANT (delocalized over 5 molecules on average); upon thermal excitation the exciton extends to two molecules while the charge expands over several molecules, and finally both exciton and charge re-localize either on a neighbouring molecule, in the exciton case, or at a position apart from the original position, in the charge carrier case.

References

- [1] Aragó, J. & Troisi, A. Regimes of exciton transport in molecular crystals in the presence of dynamic disorder. *Adv. Funct. Mater.* **26**, 2316–2325 (2016).
- [2] Yi, Y., Coropceanu, V. & Brédas, J.-L. A comparative theoretical study of exciton-dissociation and charge-recombination processes in oligothiophene/fullerene and oligothiophene/perylene diimide complexes for organic solar cells. *J. Mater. Chem* **21**, 1479 (2011).
- [3] Carmen Ruiz Delgado, M., Kim, E. G., Da Silva Filho, D. A. & Bredas, J. L. Tuning the charge-transport parameters of perylene diimide single crystals via end and/or core functionalization: A density functional theory investigation. *J. Am. Chem. Soc.* **132**, 3375–3387 (2010).
- [4] Landi, A. & Padula, D. Multiple charge separation pathways in new-generation non-fullerene acceptors: a computational study. *J. Mater. Chem. A* **9**, 24849–24856 (2021).
- [5] Klevens, H. & Platt, J. Spectral resemblances of cata-condensed hydrocarbons. *J. Chem. Phys.* **17**, 470–481 (1949).
- [6] Lambert, W., Felker, P., Syage, J. & Zewail, A. Jet spectroscopy of anthracene and deuterated anthracenes. *J. Chem. Phys.* **81**, 2195–2208 (1984).
- [7] Janssen, R., Smilowitz, L., Sariciftci, N. & Moses, D. Triplet-state photoexcitations of oligothiophene films and solutions. *J. Chem. Phys.* **101**, 1787–1798 (1994).
- [8] de Melo, J. S., Silva, L. M., Arnaut, L. G. & Becker, R. Singlet and triplet energies of α -oligothiophenes: A spectroscopic, theoretical, and photoacoustic study: Extrapolation to polythiophene. *J. Chem. Phys.* **111**, 5427–5433 (1999).
- [9] Kircher, T. & Löhmansröben, H.-G. Photoinduced charge recombination reactions of a perylene dye in acetonitrile. *Phys. Chem. Chem. Phys.* **1**, 3987–3992 (1999).
- [10] Mishra, A. *et al.* A-D-A-type S, N -Heteropentacenes: Next-Generation Molecular Donor Materials for Efficient Vacuum-Processed Organic Solar Cells. *Adv. Mater.* **26**, 7217–7223 (2014).
- [11] Zou, X. *et al.* An Insight into the Excitation States of Small Molecular Semiconductor Y6. *Molecules* **25**, 4118 (2020).
- [12] Martin, R. L. Natural transition orbitals. *J. Chem. Phys.* **118**, 4775–4777 (2003).
- [13] Cupellini, L., Caprasecca, S., Guido, C. A. & Mennucci, B. NTOBuilder - A python tool to compute NTO orbitals and related metrics. (2020). URL <https://doi.org/10.5281/zenodo.3948078>.

- [14] Yanai, T., Tew, D. P. & Handy, N. C. A new hybrid exchange–correlation functional using the coulomb-attenuating method (cam-b3lyp). *Chem. Phys. Letters* **393**, 51–57 (2004).
- [15] Improta, R., Ferrer, F. J. A., Stendardo, E. & Santoro, F. Quantum-Classical Calculation of the Absorption and Emission Spectral Shapes of Oligothiophenes at Low and Room Temperature by First-Principle Calculations. *Chem. Phys. Chem.* **15**, 3320–3333 (2014).
- [16] Chai, J.-D. & Head-Gordon, M. Long-range corrected hybrid density functionals with damped atom–atom dispersion corrections. *Phys. Chem. Chem. Phys.* **10**, 6615–6620 (2008).
- [17] Voityuk, A. A. & Rösch, N. Fragment charge difference method for estimating donor-acceptor electronic coupling: Application to dna pi-stacks. *J. Chem. Phys.* **117**, 5607–5616 (2002).
- [18] Yang, C.-H. & Hsu, C.-P. A multi-state fragment charge difference approach for diabatic states in electron transfer: Extension and automation. *J. Chem. Phys.* **139**, 154104 (2013).
- [19] Hsu, C.-P., You, Z.-Q. & Chen, H.-C. Characterization of the Short-Range Couplings in Excitation Energy Transfer. *J. Phys. Chem. C* **112**, 1204–1212 (2008).
- [20] Nottoli, M. *et al.* The role of charge-transfer states in the spectral tuning of antenna complexes of purple bacteria. *Photosynth. Res.* **137**, 215–226 (2018).
- [21] Cupellini, L., Corbella, M., Mennucci, B. & Curutchet, C. Electronic energy transfer in biomacromolecules. *Wiley Interdiscip. Rev. Comput. Mol. Sci.* **9**, 1–23 (2019).
- [22] Tölle, J., Cupellini, L., Mennucci, B. & Neugebauer, J. Electronic couplings for photo-induced processes from subsystem time-dependent density-functional theory: The role of the diabatization. *J. Chem. Phys.* **153**, 184113 (2020).
- [23] You, Z.-Q. & Hsu, C.-P. Theory and calculation for the electronic coupling in excitation energy transfer. *Int. J. Quantum Chem* **114**, 102–115 (2014).
- [24] Cupellini, L., Giannini, S. & Mennucci, B. Electron and excitation energy transfers in covalently linked donor–acceptor dyads: mechanisms and dynamics revealed using quantum chemistry. *Phys. Chem. Chem. Phys.* **20**, 395–403 (2018).
- [25] Azarias, C., Cupellini, L., Belhboub, A., Mennucci, B. & Jacquemin, D. Modelling excitation energy transfer in covalently linked molecular dyads containing a bodipy unit and a macrocycle. *Physical Chemistry Chemical Physics* **20**, 1993–2008 (2018).
- [26] Sneyd, A. J. *et al.* Efficient energy transport in an organic semiconductor mediated by transient exciton delocalization. *Sci. Adv.* **7**, eabh4232 (2021).

- [27] Prodhan, S., Giannini, S., Wang, L. & Beljonne, D. Long-range interactions boost singlet exciton diffusion in nanofibers of π -extended polymer chains. *J. Phys. Chem. Lett.* **12**, 8188–8193 (2021).
- [28] Huix-Rotllant, M., Tamura, H. & Burghardt, I. Concurrent effects of delocalization and internal conversion tune charge separation at regioregular polythiophene-fullerene heterojunctions. *J. Phys. Chem. Lett.* **6**, 1702–1708 (2015).
- [29] Farahvash, A., Lee, C.-K., Sun, Q., Shi, L. & Willard, A. P. Machine learning frenkel hamiltonian parameters to accelerate simulations of exciton dynamics. *J. Chem. Phys.* **153**, 074111 (2020).
- [30] Giannini, S. *et al.* Quantum localization and delocalization of charge carriers in organic semiconducting crystals. *Nat. Comm.* **10**, 3843 (2019).
- [31] Giannini, S., Ziogos, O. G., Carof, A., Ellis, M. & Blumberger, J. Flickering Polarons Extending over Ten Nanometres Mediate Charge Transport in High-Mobility Organic Crystals. *Adv. Theory Simul.* **3**, 2000093 (2020).
- [32] Ziogos, O. G., Giannini, S., Ellis, M. & Blumberger, J. Identifying high-mobility tetracene derivatives using a non-adiabatic molecular dynamics approach. *J. Mater. Chem. C* **8**, 1054–1064 (2020).
- [33] Kranz, J. J. & Elstner, M. Simulation of Singlet Exciton Diffusion in Bulk Organic Materials. *J. Chem. Theory Comput.* **12**, 4209–4221 (2016).
- [34] Powell, R. C. & Soos, Z. G. Singlet exciton energy transfer in organic solids. *Journal of Luminescence* **11**, 1–45 (1975).
- [35] Mulder, B. Anisotropy of light absorption and exciton diffusion in anthracene crystals determined from externally sensitized fluorescence. *Philips Res. Rep* **22**, 142–149 (1967).
- [36] Mulder, B. Symmetry of the fluorescence and absorption spectra of anthracene crystals. *J. Phys. Chem. Solids* **29**, 182–184 (1968).
- [37] Blumberger, J. Recent advances in the theory and molecular simulation of biological electron transfer reactions. *Chem. Rev.* **115**, 11191–11238 (2015).
- [38] Mani, A., Schoonman, J. & Goossens, A. Photoluminescence Study of Sexithiophene Thin Films. *J. Phys. Chem. B* **109**, 4829–4836 (2005).
- [39] Pandya, R. *et al.* Femtosecond Transient Absorption Microscopy of Singlet Exciton Motion in Side-Chain Engineered Perylene-Diimide Thin Films. *J. Phys. Chem. A* **124**, 2721–2730 (2020).
- [40] Firdaus, Y. *et al.* Long-range exciton diffusion in molecular non-fullerene acceptors. *Nat. Commun.* **11**, 5220 (2020).

- [41] Kubas, A. *et al.* Electronic couplings for molecular charge transfer: benchmarking cdft, fodft and fodftb against high-level ab initio calculations. *J. Chem. Phys.* **140**, 104105–21 (2014).
- [42] Futera, Z. & Blumberger, J. Electronic couplings for charge transfer across molecule/metal and molecule/semiconductor interfaces: performance of the projector operator-based diabatization approach. *J. Phys. Chem. C* **121**, 19677–19689 (2017).
- [43] Ziogos, O. G. *et al.* Hab79: A new molecular dataset for benchmarking dft and dftb electronic couplings against high-level ab-initio calculations. *J. Chem. Phys.* (2021).